Journal of The Electrochemical Society

Elucidating the Role of B-Site Cations toward CO_2 Reduction in Perovskite-Based Solid Oxide Electrolysis Cells

Journal of The Electrochemical Society, 2022 **169** 034532
1945-7111/2022/169(3)/034532/13/$40.00 © 2022 The Electrochemical Society ("ECS"). Published on behalf of ECS by IOP Publishing Limited

Elucidating the Role of B-Site Cations toward CO_2 Reduction in Perovskite-Based Solid Oxide Electrolysis Cells

Elif Tezel,[1,=] Dezhou Guo,[2,=] Ariel Whitten,[2] Genevieve Yarema,[1] Maikon Freire,[1] Reinhard Denecke,[3,z] Jean-Sabin McEwen,[2,4,5,6,7,z] and Eranda Nikolla[1,z]

[1]*Department of Chemical Engineering and Materials Science, Wayne State University, Detroit, Michigan 48202, United States of America*
[2]*The Gene & Linda Voiland School of Chemical Engineering and Bioengineering, Washington State University, Pullman, Washington 99164, United States of America*
[3]*Wilhelm-Ostwald-Institute for Physical and Theoretical Chemistry, Leipzig University, 04103 Leipzig, Germany*
[4]*Institute for Integrated Catalysis, Pacific Northwest National Laboratory, Richland, Washington 99352, United States of America*
[5]*Department of Physics and Astronomy, Washington State University, Pullman, Washington 99164, United States of America*
[6]*Department of Chemistry, Washington State University, Pullman, Washington 99164, United States of America*
[7]*Department of Biological Systems Engineering, Washington State University, Pullman, Washington 99164, United States of America*

Solid oxide electrolysis cells (SOECs) are promising for the selective electrochemical conversion of CO_2, or mixed streams of CO_2 and H_2O, into high energy products such as CO and H_2. However, these systems are limited by the poor redox stability of the state-of-the-art Ni-based cathode electrocatalysts. Due to their favorable redox properties, mixed ionic-electronic conducting (MIEC) oxides have been considered as promising alternatives. However, improvement of the electrochemical performance of MIEC-based SOEC electrocatalysts is needed and requires an understanding of the factors that govern their activity. Herein, we investigate the effect of B-site 3*d* metal cations (Cr, Fe, Co, Ni) of $LaBO_3$ perovskites on their CO_2 electrochemical reduction activity in SOECs. We find that their electrochemical performance is highly dependent on the nature of the B-site cation and trends as $LaFeO_3 > LaCoO_3 > LaNiO_3 > LaCrO_3$. Among these perovskites, $LaNiO_3$ is the least stable and decomposes under electrochemical conditions. *In situ* characterization and *ab initio* theoretical calculations suggest that both the nature of the B-site cation and the presence of oxygen surface vacancies impact the energetics of CO_2 adsorption and reduction. These studies provide fundamental insights critical toward devising ways to improve the performance of MIEC-based SOEC cathodes for CO_2 electroreduction.
 [DOI: 10.1149/1945-7111/ac5e9b]

Manuscript submitted January 3, 2022; revised manuscript received February 22, 2022. Published March 30, 2022. *This paper is part of the JES Focus Issue on Women in Electrochemistry.*

Supplementary material for this article is available online

Devising approaches to minimize CO_2 in the atmosphere is imperative toward reducing its irreversible environmental impacts.[1] Solid oxide electrolysis cells (SOECs) are promising systems for electrochemically converting CO_2 or mixed streams of CO_2 and H_2O into high energy products, such as CO and H_2, which can serve as precursors for production of fuels and chemicals using existing technologies, such as Fischer Tropsch. Metallic Ni/yttria stabilized zirconia (Ni/YSZ) cermet is the state-of-the-art cathode electrocatalyst for SOECs,[2] where Ni is responsible for the activation of CO_2 or H_2O, while YSZ facilitates ion transport at the triple phase boundary (interface between the metal, the oxide and the gas molecules). However, Ni/YSZ suffers from loss in long-term performance due to its limited redox stability and coking in the case of CO_2 reduction.[3,4] Other metal electrocatalysts have been proposed as alternatives to Ni (i.e., Fe) for electrochemical CO_2 reduction based on their binding strength with oxygen, which was reported as an activity descriptor.[5] However, highly active metals, such as Fe, exhibited significant redox instability and a dynamic electrochemical behavior caused by catalyst oxidation under electrochemical CO_2 reduction conditions.[6] Alloying Fe with less oxophilic metals was reported as an approach to overcome this challenge. Nevertheless the long-term stability still remained an issue.[7–10]

Mixed ionic and electronic conducting (MIEC) oxides belonging to the perovskite family have been explored as promising alternatives to 3*d* transition metal electrocatalysts due to their stable redox properties.[11–14] These oxides are of the general form ABO_3 (A refers to an alkaline earth or rare earth metal cation; B refers to a transition metal cation) and can accommodate >90% of the metals in the periodic table in their structure giving rise to a vast phase space that allows to tune their catalytic performance.[15] Although a large perovskite compositional space is available, only a narrow window has been investigated in SOECs.[11,12,14] Furthermore, direct comparison of the performance of the reported perovskite compositions for CO_2 electrolysis from the literature presents challenges due to variations in testing parameters among various studies. Nevertheless, some general trends can be derived. For example, the perovskite B-site transition metal cations have been largely considered as being responsible for the catalytic activity toward CO_2 reduction and electron transfer.[16–18] $La_{0.75}Sr_{0.25}Cr_{0.5}Mn_{0.5}O_3$ (LSCM) perovskite is one of the most studied MIEC electrocatalysts as an alternative to the Ni/YSZ cermet for CO_2 reduction in SOECs because of the excellent stability in redox cycles.[12,13,19–23] However, LSCM suffers from limited electrocatalytic activity as compared to Ni/YSZ-based cermet SOEC cathodes.[24] Ishihara and co-workers[11] examined different MIEC oxides, including three perovskites and three Ruddlesden-Popper (R-P) oxides with varying compositions as cathode electrocatalysts for CO_2 reduction under a 100 ml min^{-1} flow of 50% CO_2:1% CO balanced in Ar at 1073 K using a similar SOEC cell structure (MIEC Oxide or $NiO|La_{0.9}Sr_{0.1}Ga_{0.8}Mg_{0.2}O_3|Ba_{0.6}La_{0.4}CoO_{3+\delta}$). The performance trend reported for these oxides was $La_{0.6}Sr_{0.4}FeO_{3-\delta} > Sr_3Fe_2O_{7-\delta} > LaFeO_{3-\delta} > Ce_{0.6}Mn_{0.3}Fe_{0.1}O_{2-\delta} > La_{1.8}Sr_{0.2}NiO_{4+\delta} > La_2NiO_{4+\delta} > SrZr_{0.8}Ni_{0.2}O_{3-\delta}$. The best performing MIEC oxides contained Fe as the B-site cation, suggesting that the Fe cations were responsible for the enhanced catalytic turnover. Substituting the La A-site with Sr in Fe-based perovskites increased the electrochemical rates for CO_2 electrolysis ($LaFeO_{3-\delta}$, current density of 136 mA cm^{-2} vs $La_{0.6}Sr_{0.4}FeO_{3-\delta}$ of 187 mA cm^{-2} at 1.6 V). This was linked to (i) an increase in the oxygen non-stoichiometry (delta, δ) upon A-site doping with Sr due to the difference in the valence state of the A site cations (Sr^{2+} vs La^{3+}), and (ii) an enhancement in the electronic conductivity, induced by an increase in the electron-hole concentration and straightening of the O-B-O bond, resulting in improved orbital overlapping between B-3*d* and O-2*p*.[25,26]

[=]These authors contributed equally to this work.
[z]E-mail: denecke@uni-leipzig.de; js.mcewen@wsu.edu; erandan@wayne.edu

In another study, the surface chemistry of CO_2 reduction on $La_{0.6}Sr_{0.4}FeO_{3-\delta}$ was investigated by Opitz et al.[27] along with $(La_xSr_{0.2})(Cr_{1-y}Ni_y)O_{3-\delta}$ (x = 0.8, 0.7; y = 0, 0.1) perovskites at SOEC operating temperatures using near-ambient pressure X-ray photoelectron spectroscopy (NAP-XPS). This study showed that CO_2 electrolysis on all investigated MIECs proceeded via the formation of a carbonate intermediate, which formed via adsorption of CO_2 on a surface oxygen vacancy through an electron transfer, suggesting that the surface oxygen vacancies were mainly responsible for CO_2 adsorption.[27] Another work from Ren et al. reported a systematic density functional theory (DFT) study of the CO_2 adsorption and reduction mechanisms on (001) FeO_2-terminated surface models of $La_{0.5}Sr_{0.5}Fe_{1-x-y}Ni_xMn_yO_{3-\delta}$ (x, y = 0, 0.125, 0.25) with varying surface oxygen vacancy concentrations.[28] They concluded that an oxide ($La(Sr)Fe_{0.75}Ni_{0.125}Mn_{0.125}O_{2.75}$) with mixed B-site cations of varying oxophilicity (Mn vs. Ni) and two adjacent surface oxygen vacancies would lead to the most active surface for CO_2 electrolysis. In general, these literature reports suggest implication of the B-site cations and/or oxygen surface vacancies of MIEC-based electrocatalysts in the activation of CO_2 in SOECs, however a clear discrimination of these effects is still elusive.

Herein, we investigate the effect of the B-site, 3*d* transition metal cations of La-based perovskites ($LaBO_3$; B = Fe, Co, Ni and Cr) on the electrochemical CO_2 reduction in SOECs. We correlate changes in the B-site cation composition to the adsorption and activation energetics of CO_2 by coupling *in situ* CO_2 Diffuse Reflectance Infrared Fourier Transform Spectroscopy (DRIFT) studies and DFT-based calculations. We also study the effect of oxygen vacancies in these oxides on the CO_2 adsorption and activation via DFT calculations. The electrochemical performance is evaluated using a combination of electrochemical chronoamperometric and impedance studies. Faradaic efficiency toward CO production is determined through determination of the product distribution using on-line gas chromatography.

Experimental

Catalyst synthesis.—ABO_3 (A = La; B = Fe, Co, Ni and Cr) perovskites were synthesized using a sol-gel method.[29,30] Initially, precursors were prepared by dissolving stoichiometric amounts of metal nitrates (i.e., $La(NO_3)_3{\cdot}6H_2O$ and $Fe(NO_3)_3{\cdot}9H_2O$ or $Ni(NO_3)_2{\cdot}6H_2O$ or $Co(NO_3)_2{\cdot}6H_2O$ or $Cr(NO_3)_2{\cdot}3H_2O$) in deionized water at room temperature, followed by stirring. The appropriate amount of citric acid was added to the mixture as a complexing agent, and the molar ratio of metal ions to citric acid was kept at 1:1.1. This was followed by continuously stirring the mixture at 85 °C until the gelation process was completed by water removal. The resulting gel was heated from room temperature to 400 °C using a heating rate of 3 °C min^{-1} under an air flow to remove evolved gas phase species. The sample was then combusted at 400 °C for 3 h to remove the complexing agent. The resulting powder was crushed prior to calcination at 750 °C for 5 h to achieve the appropriate oxide crystal structure.

Electrochemical cell synthesis.—Electrolyte-supported electrochemical cells were fabricated by initially sieving the appropriate amount of $La_{0.9}Sr_{0.1}Ga_{0.8}Mg_{0.2}O_3$ (LSGM) powder using a 125 μm sieve and pressing the powder into 13 mm diameter pellets. This was followed by sintering of the pellets in air at 1450 °C for 5 h. This led to an electrolyte layer with a thickness of ~400 μm and a diameter of 10 mm. The anode was prepared by ball milling a mixture of LSGM-LSCF ($La_{0.6}Sr_{0.4}Co_{0.2}Fe_{0.8}O_3$), polyvinyl butyral (PVB), poly(ethylene-propylene glycol) (UCONN), butyl benzyl phthalate (BBP) and fish oil in ethanol for 36 h. LSCF was prepared prior to ball milling using a sol-gel method as detailed in the Supplementary Material (available online at stacks.iop.org/JES/169/034532/mmedia). The slurry was then spray-coated onto one side of the LSGM electrolyte, and the cells were sintered at 1000 °C for 2 h. Lastly, the cathode was prepared via spray coating, with a milled mixture of $LaBO_3$, PVB, UCONN, BBP and fish oil in ethanol. The cell was then sintered at 950 °C for 2 h. The oxide loading (~2 mg) on the cathode was kept similar among the different perovskites. Au mesh (Precision Eforming, NY) and wires (Alfa Aesar) were used as current collectors for both electrodes. Conductive Au paste (TED Pella) was applied to affix the cell connections.

Characterization.—The crystal structure and phase formation of the as-synthesized oxides were examined using an X-ray diffractometer (XRD) (D2 Phaser, Bruker Corporation) employing Cu K_α radiation (1.54 Å) in the 2θ range of 20 to 80° with a step size of 0.01°. The oxidation states of the metals in the oxides were determined via an X-ray photoelectron spectrometer (XPS) (Thermo Fisher NEXSA, monochromatic Al K_α source with an energy of 1486.6 eV). The measurements were performed with a step size of 0.1 eV. Pass energies for the survey scans and the high-resolution analysis (HR-XPS) were 160 eV and 25 eV, respectively. La 4*d* and Ni 3*p* core level regions were chosen for analysis due to the overlap between La 3*d* and Ni 2*p* spectra. Data were analyzed using the CasaXPS software, and a Shirley type background was used in all analyses. Electron micrographs were collected using a field-emission scanning electron microscope (FE-SEM, JSM 7600, JEOL Inc., Japan) at an accelerating voltage of 15 kV and a working distance of ~8 mm. To prevent charging due to the electron beam, samples were sputtered with a thin layer of Au, prior to loading onto the microscope chamber. High angle annular dark field-scanning tunneling electron microscopy (HAADF-STEM) images were collected using a Talos F200X microscope (Thermo Fisher Scientific, USA) equipped with a field emission electron source.

The specific surface areas of the oxides were calculated by the Brunauer–Emmett–Teller (BET) method using a Micromeritics ASAP 2020. Before analysis, the samples were consistently degassed at 350°C for 90 min, followed by nitrogen physisorption at 77 K. Iodometric titrations were used to determine the oxygen non-stoichiometry (delta, δ) of the perovskites. They were performed using an excess amount of potassium iodide (KI) and hydrochloric acid (HCl). Approximately 20–30 mg of $LaBO_{3-\delta}$ was mixed with ~0.52 g of KI and approximately 5.0 g of water. The mixture was bubbled under Argon to remove any oxygen in the vessel. Following this, 5 ml of 2 M HCl (12 M for $LaFeO_{3-\delta}$) were added to digest the perovskite, yielding a strong yellow/brownish solution. The titration was then started using a 0.01 M sodium thiosulfate ($Na_2S_2O_3$) solution until the yellow color became pale. At this point, 1 ml of saturated starch solution was added, generating a dark blue/black-colored solution. Once again, the solution was titrated until the solution became colorless. The amount of titrant consumed during each titration was used to determine the oxidation state of the B-site transitional metal cations, from which the oxygen non-stoichiometry (δ) was calculated.

Electrochemical testing.—All electrochemical studies were performed using a Gamry 300 potentiostat (Gamry Inst. Warminster, PA). Linear sweep voltammetry measurements were conducted using a sweep rate of 10 mV s^{-1} in electrolysis mode with the anode exposed to nitrogen and the cathode exposed to a gas mixture of 10% CO_2:3% CO balanced in N_2 at a total flow rate of 50 ml min^{-1} (5 ml min^{-1} CO_2: 1.5 ml min^{-1} CO: 43.5 ml min^{-1} N_2). Electrochemical impedance spectra (EIS) were collected for the cells measured under an ac potential with a frequency range of 1 MHz to 0.01 Hz and an amplitude of 20 mV at different applied voltages at 800 °C under a 50 ml min^{-1} flow of 10% CO_2:3% CO balanced in N_2. The total non-ohmic electrode polarization resistances were obtained from multiplying the real axis of the raw complex resistance (excludes ohmic resistance) with the electrode geometric interfacial area (S = 0.1 cm^2). An equivalent circuit model was fitted to the experimental impedance spectra obtained from a $LaFeO_3$ cathode-based cell as an example to deconvolute the total non-ohmic polarization resistance using the Gamry EIS300 Electrochemical

Impedance Spectroscopy Software. The generated current densities for all cells were measured in chronoamperometry mode at different applied voltages (1.1, 1.3, 1.5 V) at 800 °C and the outlet gas stream from the cathode compartment was analyzed using a gas chromatograph (Shimadzu, GC 2014) to detect CO production as a function of applied voltages. The Faradaic efficiency to CO was calculated as the ratio of the total moles of supplied electrons to the moles of electrons needed to generate the amount of CO detected by the GC.

DRIFT studies.—Diffuse reflectance infrared Fourier transform (DRIFT) spectra were obtained using a FT-IR NICOLET 8700 (Thermo Fisher Scientific) spectrometer equipped with a high temperature Harrick Praying Mantis Diffuse Reflectance cell. The Nicolet OMNIC software was used to convert the absorbance data into Kubelka−Munk (KM) format. DRIFT experiments were performed using mechanically mixed 20 percent by weight perovskite in KBr. Prior to the measurements, residual surface species were removed by heating the sample up to 500°C under a pure O_2 flow for 3 h at 50 ml min^{-1}. The gas flow was then switched to helium for 2 h to flush out the system of any gas phase or absorbed oxygen species. The temperature was then cooled to 300 °C, and a 50 ml min^{-1} flow of 10% CO_2:90% He gas mixture was introduced for 30 min. This was followed by cooling the cell to room temperature under helium flow and flushing the system prior to the measurements. DRIFT measurements were conducted with a 4 cm^{-1} resolution in the 4000−650 cm^{-1} spectral range, averaging over 64 scans at room temperature.

Computational Details

Theoretical calculations were preformed using the Vienna *Ab initio* Simulation Package (VASP)[31] and the Revised Purdue-Burke-Erzenholf functional was used to simulate adsorption configurations of CO_2 on model $LaCoO_3$, $LaFeO_3$ and $LaNiO_3$ surfaces.[32] These calculations utilize the planewave basis sets with Projector Augmented Wave (PAW) potentials[33,34] released in 2017. For all surface calculations, a 4 × 4 × 1 **k**-point Monkhorst-Pack grid was used to sample the first Brillouin zone. Gaussian smearing was employed with a width of 0.05 eV and a convergence criterion was 10^{-6} eV and 0.03 eV $Å^{-1}$ for electronic energies and interatomic forces on the relaxed layers, respectively. The structure visualizations were performed with VESTA.[35]

Due to the superexchange interaction that is observed when cations within the crystalline field are surrounded by octahedral or tetrahedral anion configurations, these perovskite surfaces exhibit antiferromagnetic ordering (AFM).[36–38] Previous literature has investigated the effects of AFM ordering on bulk perovskite structures. In a study conducted by Curnan et al., they found that although necessary for the characterization of orbital energetics, the application of AFM ordering did little to change the oxygen vacancy formation energy.[39] Furthermore, studies conducted on $LaCoO_3$ have shown that when using the RPBE functional the ground state of $LaCoO_3$ is nonmagnetic and will only exhibit AFM ordering when utilizing higher level functionals.[40] To simplify the calculations conducted in this project, AFM ordering will be omitted as it complicates the calculations without drastically changing the energetics of forming an oxygen vacancy which has been attributed to increased affinity for activation of CO_2.

The $LaCoO_3$, $LaFeO_3$ and $LaNiO_3$ surfaces were constructed based on their corresponding perovskite crystalline structures. A (8 × 8 × 8) Monkhorst-Pack k-point mesh was used for $LaCoO_3$ and $LaNiO_3$, and a (8 × 8 × 6) mesh for $LaFeO_3$ in determining the optimized bulk phase lattice. The optimized $LaCoO_3$ cell parameters were $a = b = c = 5.40$ Å from the DFT simulations as compared to $a = b = c = 5.48$ Å as obtained from the X-ray experimental values.[41] The optimized $LaNiO_3$ cell parameters were $a = b = c =$ 5.47 Å from the DFT simulations as compared with the experimental values of $a = b = c = 5.44$ Å[42]; the optimized $LaFeO_3$ cell parameters were $a = 5.47$ Å, $b = 5.49$ Å, $c = 7.76$ Å from the DFT simulations, which were comparable to the experimental values of $a = 5.60$ Å, $b = 5.66$ Å, $c = 7.94$ Å.[43]

We examined various facets for each perovskite structure (as shown in Fig. S1 in the Supplementary Material) and chose the energetically most favorable surface orientations, i.e., the (001) surface for $LaNiO_3$, the (110) surface for $LaCoO_3$, and (001) surface for $LaFeO_3$ as shown in Fig. 1, for determining the adsorption energetics of CO_2. The surface energies were calculated as:

$$\gamma = \frac{E_{LaBO_3}^{unrelaxed} - N_{bulk}E_{bulk}}{2A} + \frac{E_{LaBO_3}^{relaxed} - E_{LaBO_3}^{unrelaxed}}{A} \quad [1]$$

herein, $E_{LaBO_3}^{unrelaxed}$ is the final energy of the first geometric step in the surface geometry optimization, $E_{LaBO_3}^{relaxed}$ is the final energy of the relaxed structure, and A is the surface area of the p (1 × 1) unit cell. The value of A is determined from the optimized bulk unit cell parameters. As for N_{bulk}, it is the number of bulk unit cells that are contained within the slab with a corresponding energy of E_{bulk}.

Each oxide surface was modeled in a p (1 × 1) 6-layer surface. The top two layers of the surface were relaxed to model the surface-adsorbate interactions, while the bottom four layers were fixed at their optimized bulk values. A vacuum layer of around 10 Å with a dipole correction along the z-direction was used to prevent the interaction of the top and bottom layers of the surface.

Adsorption studies of CO_2 were conducted using the optimized surfaces of the abovementioned perovskites. The adsorption energies of CO_2 were determined using the following equation:

$$E_{ads} = E_{CO_2/LaBO_3} - E_{LaBO_3} - E_{CO_2(g)} \quad [2]$$

where E_{ads} is the adsorption energy of CO_2, $E_{CO_2/LaBO_3}$ is the energy of the surface with CO_2 adsorbed onto it, E_{LaBO_3} is the energy of the surface and $E_{CO_2(g)}$ is the energy of CO_2 in the gas phase. We note here that the calculations were performed at a saturation coverage of CO_2, which we define to be 1 ML. Indeed, although there are four lattice oxygen species in a p (1 × 1) unit cell that the carbon in the CO_2 molecule could potentially chemisorb to form a carbonate species, the proximity of the lattice oxygen species within this unit cell is such that one can only accommodate one CO_2 adsorbate.

The electronic interactions between the molecule (CO_2) and the perovskite surface were also quantified through the differential charge density, which quantifies the movement of electrons in the system as the molecule adsorbs onto the surface. The differential charge density was calculated according to:

$$\Delta\rho(\vec{r}) = \rho_{total}(\vec{r}) - \rho_{molecule}(\vec{r}) - \rho_{surface}(\vec{r}) \quad [3]$$

where $\rho_{total}(\vec{r})$, $\rho_{molecule}(\vec{r})$ and $\rho_{surface}(\vec{r})$ are the charge distribution for the whole system, the gas phase molecule and the bare catalyst surface, respectively. Based on the differential charge of the electron density, we then integrated over the unit cell to give us the mean absolute charge transferred between the adsorbate and the surface (Q):

$$Q = \frac{1}{2}\int dr|\Delta\rho(\vec{r})| \quad [4]$$

To provide a detailed identification of the adsorbate at specific adsorption sites, we calculated the harmonic vibrational frequencies of CO_2 on the perovskite surfaces using finite differences on the forces with displacements of 0.02 Å. When more than one stable adsorption configuration was found, we averaged of the frequency dependence of the intensities for each adsorption configuration to accurately compare the experimental DRIFTS spectra and the theoretical spectra, as detailed the Supplementary Material. Further, to verify whether the simulated IR spectra were affected by the small size of the p (1 × 1) unit cell that was used, we also simulated the IR spectra within a p (2 × 2) unit cell at the same CO_2

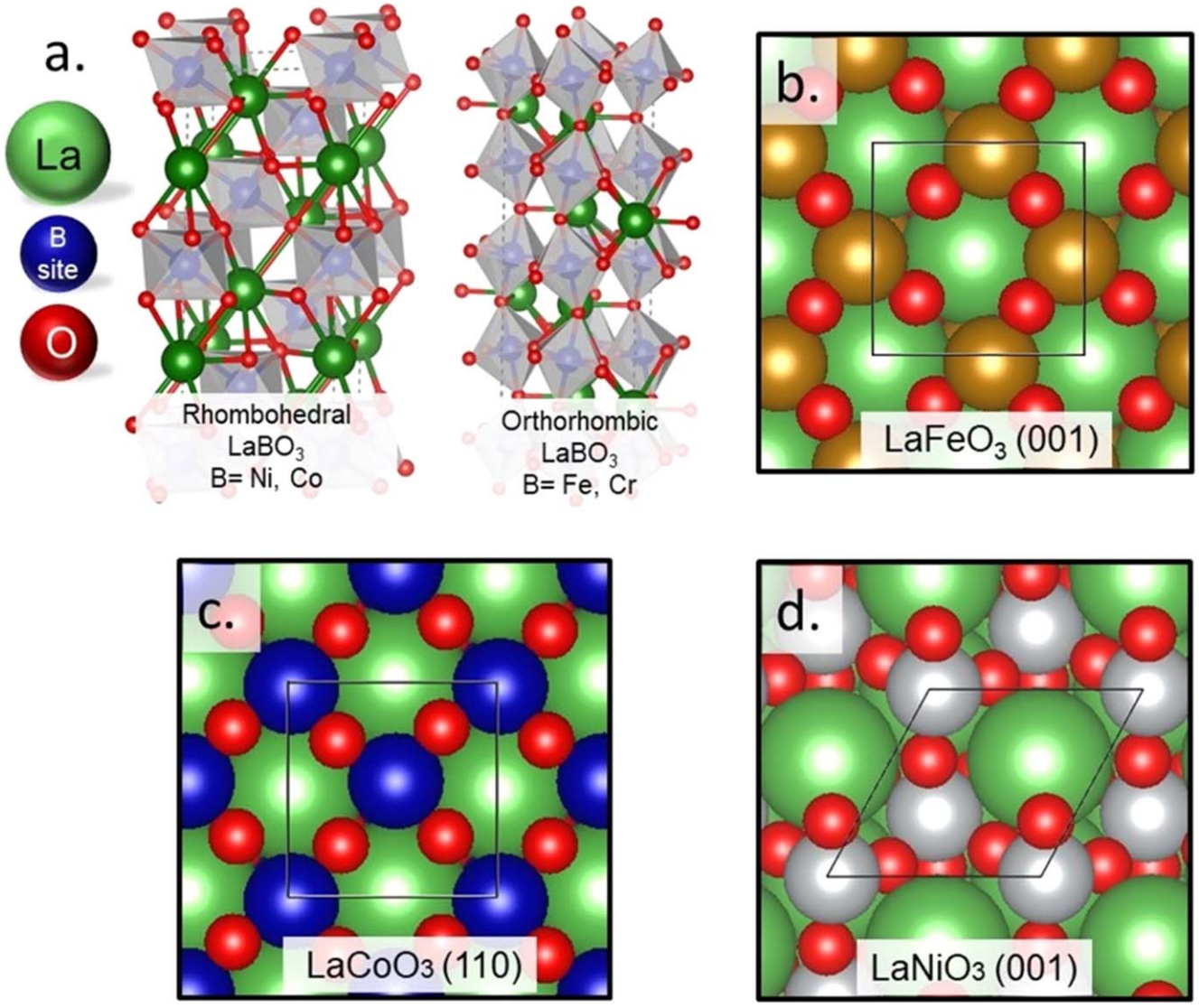

Figure 1. (a) Crystal structure models of rhombohedral and orthorhombic $LaBO_3$. Top view of the (b) $LaFeO_3$ (001) surface; (c) $LaCoO_3$ (110) surface; (d) $LaNiO_3$ (001) surface. The La, O, Fe, Co and Ni atoms or ions are represented by green, red, bronze, blue and silver spheres, respectively.

coverage of 1 ML for the $LaFeO_3$ system (which was sampled using a 2 × 2 × 1 **k**-point Monkhorst-Pack grid). To determine the adsorption energetics of CO_2 on the perovskite surfaces, the transition-state calculations were performed with the climbing image nudge elastic band (CI-NEB) method by finding the saddle points and minimum energy paths between the physiosorbed and chemisorbed CO_2 configurations. A number of intermediate images were optimized along the reaction path, with the constraints implemented by adding spring forces along the band between images and projecting out the component of the force because the potential is perpendicular to the band. The number of images was adjusted specifically for transition-state calculation such that the tangent along the path was well described. Four images were used in these calculations. The structural optimization was performed until the forces acting on the atoms on the images were smaller than 0.03 eV/Å.

Results and Discussion

Electrocatalyst characterization.—A series of ABO_3 (A = La; B = Fe, Co, Ni and Cr) perovskites were synthesized consistently using a sol-gel approach. The particle characteristics, crystal structure and phase formation of the synthesized perovskites were examined using high annular dark field tunneling electron microscopy (HAADF-STEM) and powder X-ray diffraction (XRD). Figures 2a–2c show HAADF-STEM images of the as-synthesized perovskite particles at different resolutions, confirming the ordering of the atoms in a rhombohedral $LaBO_3$ structure with La lattice spacing of 4 Å, as an example. Figure 2d shows the XRD patterns of rhombohedral $LaNiO_3$ with space group R3c̄, rhombohedral $LaCoO_3$ with space group R3c̄, orthorhombic $LaFeO_3$ with space group Pnma, and orthorhombic $LaCrO_3$ with space group Pnma, confirming pure phase crystallinity of all the perovskite structures synthesized.

The physical surface areas of the synthesized oxides were measured using N_2 physisorption via the standard Brunauer–Emmett–Teller (BET) method and determined to be 5 ± 0.7 $m^2\ g^{-1}$ for all perovskites considered. Also, iodometric titration studies indicated δ's of 0.024 ± 0.007, 0.026 ± 0.004 and 0.017 ± 0.008 for $LaNiO_{3-\delta}$, $LaCoO_{3-\delta}$ and $LaFeO_{3-\delta}$ perovskites, respectively. Similar δ values for these perovskites have been reported previously.[44–46] In the case of $LaCrO_3$, the determination of δ by titration was not possible due to difficulties with complete digestion of this perovskite in acid, and the limited ability of Cr^{3+} to oxidize I^{3-} ions even if complete digestion in acid was achieved.[47] The cross-sectional SEM of the $LaBO_3$-based SOEC cathode is shown in Fig. 2e, confirming the porous and uniform structure of the electrode. Figure S2 shows the cross-sectional SEM of

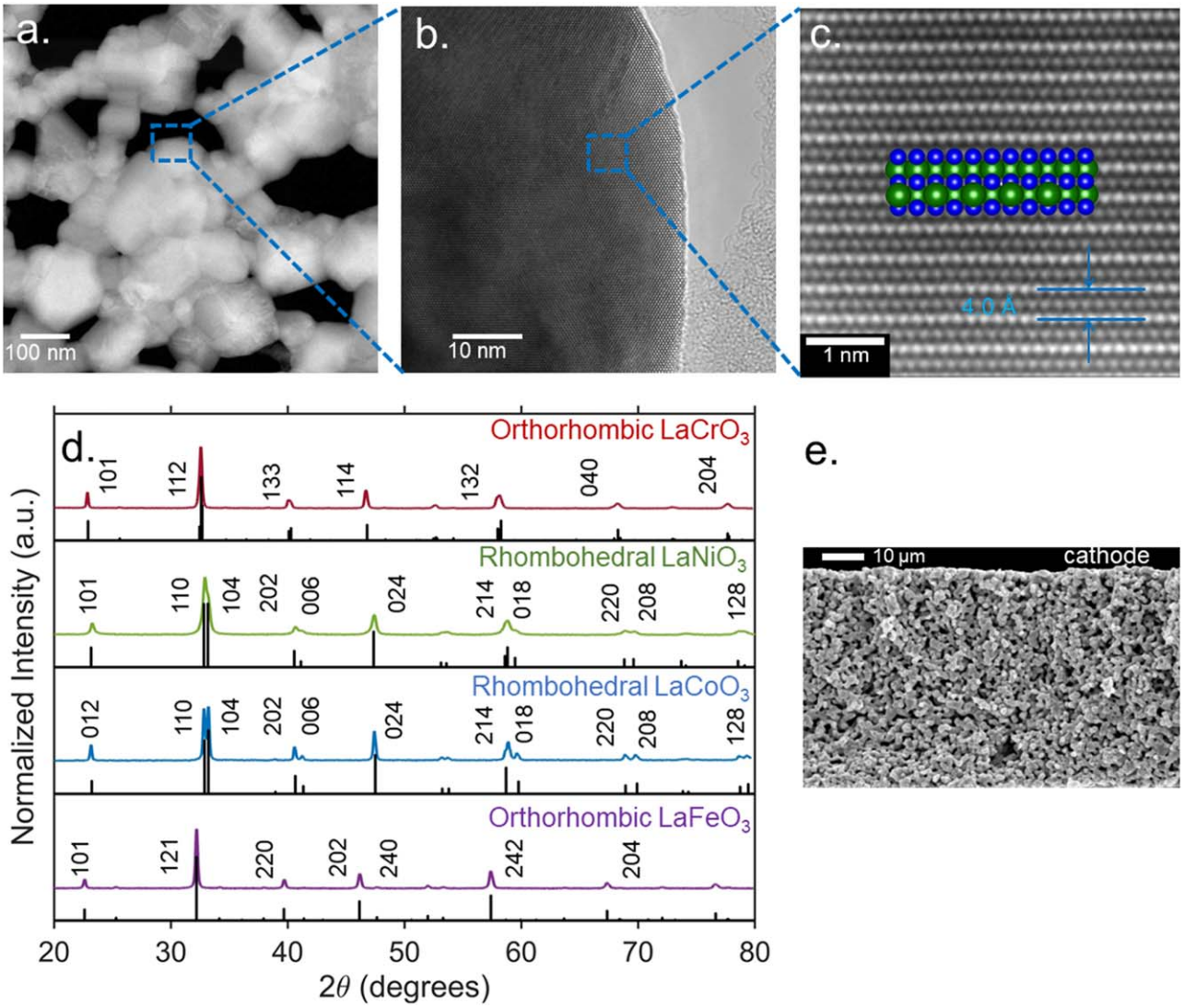

Figure 2. (a) HAADF-STEM micrograph of $LaBO_3$ particles. (b) A high resolution STEM micrograph of the region boxed in (a). (c) Atomic resolution HAADF-STEM micrograph of the region boxed in (b). Green and blue spheres in the inset model represent A- and B-site cations, respectively. (d) XRD patterns for orthorhombic $LaCrO_3$, rhombohedral $LaNiO_3$, rhombohedral $LaCoO_3$, and orthorhombic $LaFeO_3$. The respective reference spectra are shown in black (e) A cross-sectional SEM of the $LaBO_3$-based SOEC cathode.

the entire cell used in these studies composed of a 400 μm LSGM electrolyte, which physically supported the anode and the cathode.

Electrocatalytic performance.—The effect of the B-site composition of $LaBO_3$ (B = Ni, Co, Fe, Cr) oxides on the electrochemical performance toward CO_2 reduction was examined using linear sweep voltammetry measurements (current-voltage (I–V) behavior) of SOECs containing $LaBO_3$ at the cathode under a 50 ml min^{-1} flow of 10% CO_2:3% CO balanced in N_2 at 800 °C (Fig. 3a). The perovskite weight loading at the cathode was kept comparable among the different perovskites, given the similarity in their physical surface areas. For analysis, the generated currents were normalized by the geometric area of the cathode. The current-voltage (I-V) profiles for SOECs containing different $LaBO_3$ perovskites, shown in Fig. 3a, indicate that the activation overpotential losses (in the low potential region < 1.1 V) were significantly impacted by the nature of B-site 3*d* transitional metal cation in these oxides. The generated current density at 1.1 V was the highest for the $LaFeO_3$-based SOEC (112 mA cm^{-2}) followed by $LaCoO_3$ (90 mA cm^{-2}), $LaNiO_3$ (23 mA cm^{-2}) and $LaCrO_3$ (8 mA cm^{-2}) based cells. The SOECs containing $LaNiO_3$ and $LaCrO_3$ showed very limited activity toward CO_2 reduction. We note that current generation below the theoretical potential (~0.88 V) for CO_2 reduction under the reported conditions was observed for some of these oxides due to the mobility of oxygen leading to oxide reduction. The extent of current generation in this regime scaled with the oxide reducibility.[29] The most reducible oxide among those considered, $LaNiO_3$, exhibited the most significant current generation, which as we show below was detrimental at maintaining a stable oxide structure under electrochemical conditions. In the case of $LaFeO_3$ and $LaCoO_3$, the current generated below the theoretical potential was limited, however, it would suggest formation of oxygen vacancies in these oxides under an applied potential. In the case of $LaCrO_3$, the current generation was negligible consistent with its limited reducibility under the conditions considered. These observations indicate potential implication of the surface oxygen defects generated under an applied potential in the case of $LaFeO_3$ and $LaCoO_3$ on their electrochemical performance toward CO_2 reduction. We anticipate that the application of an external electric field will also affect the adsorption of CO_2. In our previous work on yttrium stabilized zirconia, we found that the presence of a negative electric field could strengthen the adsorption of CO_2. The presence of a positive electric field also affected its adsorption strength, although its effect was not as significant as in the presence of a negative field.[48]

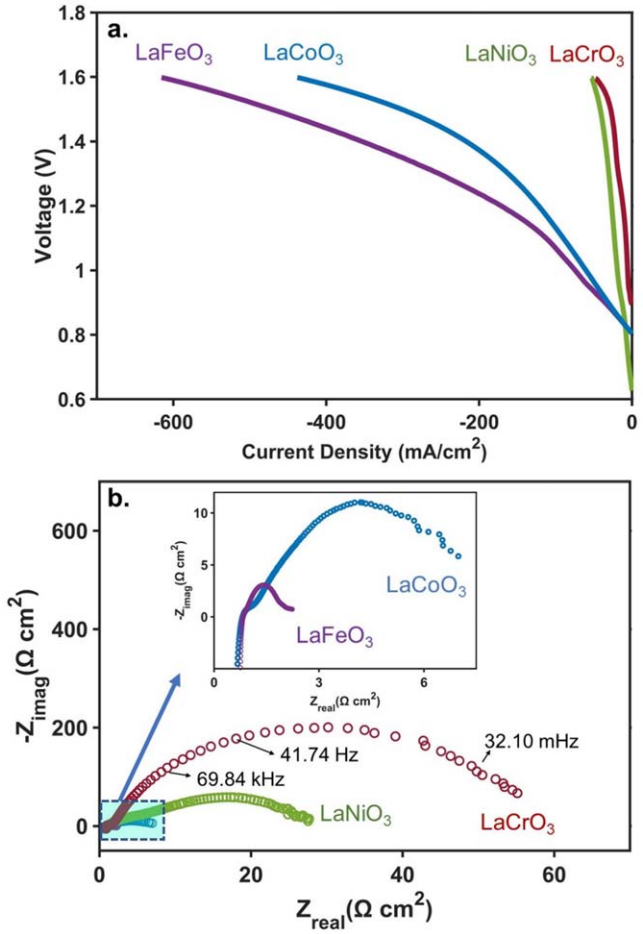

Figure 3. (a) Current-voltage (I−V) profiles of SOECs with $LaFeO_3$/LSGM (purple), $LaCoO_3$/LSGM (blue) and $LaNiO_3$/LSGM (green) and $LaCrO_3$/LSGM (red) cathodes in electrolysis mode. (b) Impedance spectra for $LaBO_3$|LSGM|LSCF cells at an applied voltage of 1.1 V. Inset: Magnified spectra of cells containing $LaFeO_3$ and $LaCoO_3$. All electrochemical tests were performed under a 50 ml min^{-1} flow of 10% CO_2:3% CO balanced in N_2 at 800 °C.

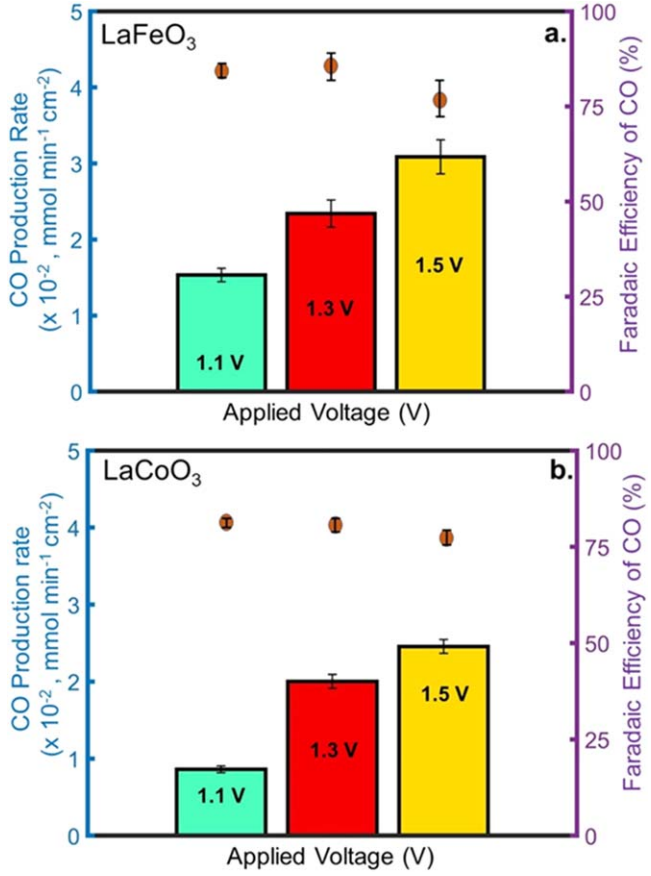

Figure 4. CO production rates and Faradaic efficiency of CO for SOECs with cathodes composed of (a) $LaFeO_3$ and (b) $LaCoO_3$. The bar graphs (left axis) represent CO production rates, while the scatter graph represents Faradaic efficiency of CO (right axis).

Electrochemical impedance spectra (EIS) for SOECs measured at an applied voltage of 1.1 V at 800 °C under a 50 ml min^{-1} flow of 10% CO_2:3% CO balanced in N_2 are shown in Fig. 3b. The real-axis intercept is attributed to the ohmic polarization of the cell, which is associated with the ohmic losses due to transport of charged species. Figure 3b clearly shows that the ohmic losses were similar for all the cells. The imaginary resistance arcs are attributed to non-ohmic electrode polarization resistances arising from both electrodes. The overall non-ohmic electrode polarization resistances were calculated from normalization of the real axis of the raw complex resistance (excluding ohmic resistance) by the electrode geometric interfacial area (S = 0.1 cm^2). The overall non-ohmic electrode polarization resistances were determined to be 1.5, 6.4, 28.5 and 54.2 Ω cm^2 for SOECs containing $LaFeO_3$, $LaCoO_3$, $LaNiO_3$ and $LaCrO_3$, respectively. These non-ohmic electrode polarization resistances largely depended on the cathode electrocatalyst, suggesting that variations in the B-site of the perovskite at the SOEC cathode significantly affected the overall polarization resistances of the cell, with $LaCrO_3$ and $LaFeO_3$ exhibiting the highest and the lowest polarization resistances, respectively. Fitting of EIS using an equivalent circuit model adapted from literature[9] (Fig. S3 in Supplementary Material), suggests that the overall non-ohmic electrode polarization resistance was comprised of: (i) a high frequency resistance arc characteristic of the electrochemical processes at the anode, and (ii) a dominant low frequency arc characteristic of the electrochemical processes at cathode. This assignment was confirmed by the fact that the changes in the cathode perovskite electrocatalyst mainly affected the dominant low frequency polarization resistance arc.

Chronoamperometric constant current experiments were performed at 800 °C in a 50 ml min^{-1} flow of 10% CO_2:3% CO balanced in N_2 at different applied voltages (1.1, 1.3, and 1.5 V) to determine the selectivity toward CO production and evaluate the Faradaic efficiency. In these studies, we focused on the best performing cells with $LaCoO_3$- and $LaFeO_3$-based cathodes, since SOECs containing $LaNiO_3$ and $LaCrO_3$ at the cathode, generated very low currents and led to marginal amounts of CO production that were difficult to quantitatively analyze. Consistent with the increase in the electrochemical rates, an increase in applied voltage increased the generated current density, thus leading to an increase in CO production for both $LaCoO_3$- and $LaFeO_3$-based SOECs (Figs. 4a and 4b, respectively). The CO production rates for the $LaFeO_3$-based cell were higher than those of the $LaCoO_3$-based cells at all applied voltages, consistent with the linear sweep voltammetry studies above. No significant differences were detected in the Faradaic efficiency toward CO production between SOECs containing $LaFeO_3$ and $LaCoO_3$, which were 84 ± 1.7 and 80.5 ± 0.8% at 1.1 V, respectively. This suggests that for these high-performing SOECs the selectivity toward CO production was not significantly impacted by the B-site composition of the perovskite electrocatalyst at the cathode. A slight decrease in the Faradaic efficiency was observed for both cells as the applied voltage was increased from 1.3 V to 1.5 V. This was potentially due to the local depletion of CO_2 on the perovskite surface because of high currents generated at high voltages.[21,24,49] This could have resulted in the over-reduction of the oxide in the presence of electrons leading to lowering of the Faradaic

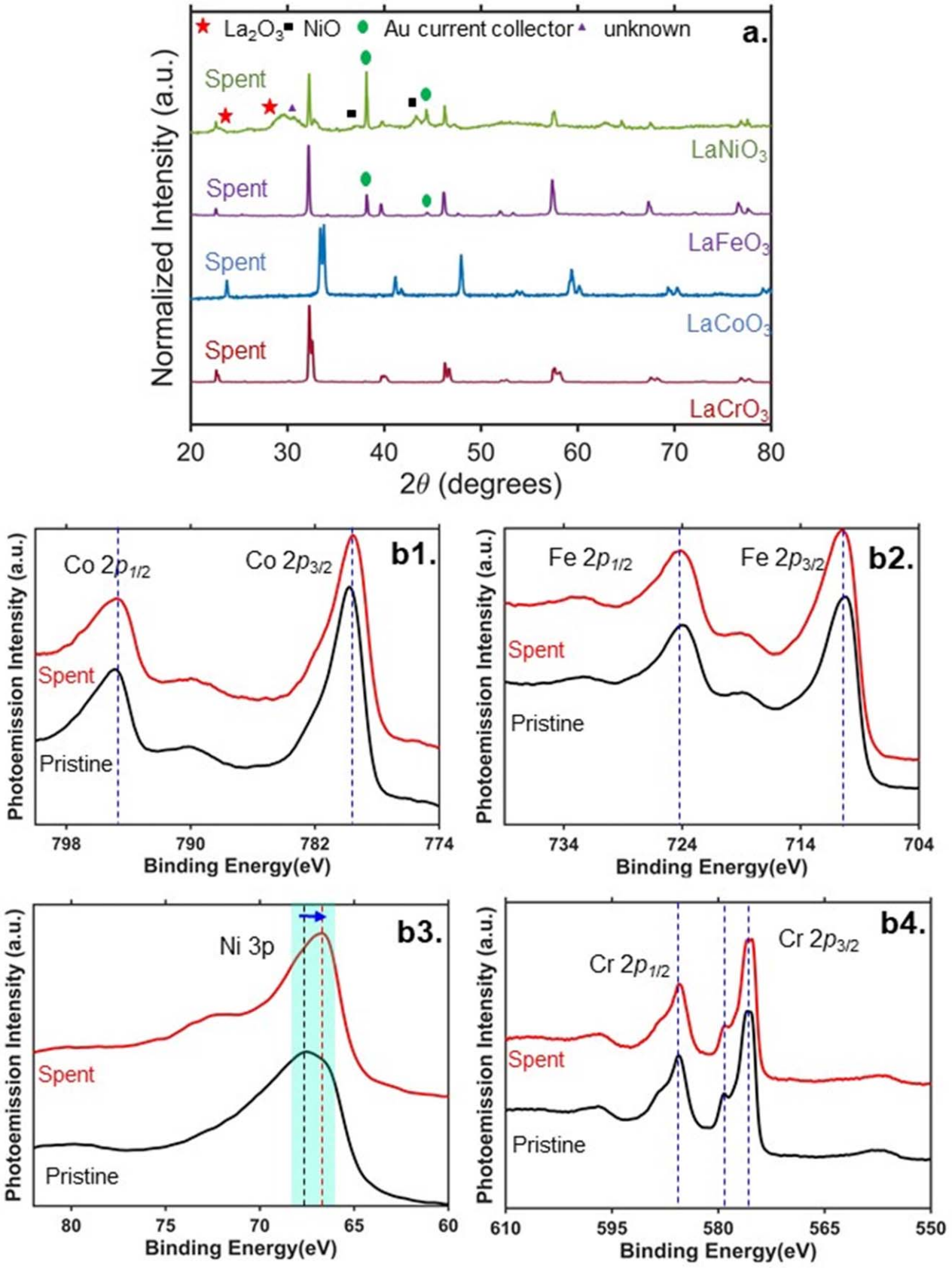

Figure 5. (a) Post-reaction XRD of SOEC cathodes containing different $LaBO_3$ oxides. (●) represents the peaks associated with Au, which is used as the current collector in the cell assembly, (★, ■ , ▲) represent diffraction peaks associated with La_2O_3, NiO and unidentified phases arising from $LaNiO_3$ decomposition under electrochemical conditions. (b) Comparison of the HR-XPS spectra before and after reaction: (b1) Co 2*p* core level spectra for SOECs containing $LaCoO_3$; (b2) Fe 2*p* core level spectra for SOECs containing $LaFeO_3$; (b3) Ni 3*p* core level spectra for SOECs containing $LaNiO_3$. Green highlighted regions in (b3) shows the peak shift in Ni 3*p* to lower binding energy after electrochemical testing.; (b4) Cr 2*p* core level spectra for SOECs containing $LaCrO_3$.

efficiency toward CO; however, this oxide over-reduction was reversible since no change in the oxide structure was detected by post-reaction characterization of $LaFeO_3$ and $LaCoO_3$ -based cathodes (Fig. 5).

Characterization of the cells containing different $LaBO_3$ perovskites at the cathode post electrochemical testing using XRD showed that $LaNiO_3$ partially decomposed to La_2O_3 and NiO oxide during electrochemical testing (Fig. 5a). This is consistent with the high reducible nature of $LaNiO_3$ characterized by weak B-O lattice bonds as we have previously reported,[29] leading to its instability under reducing electrochemical conditions when exposed to 50 ml min^{-1} flow of 10% CO_2:3% CO balanced in N_2 at 800 °C. Conversely, no significant changes were detected for $LaCoO_3$-, $LaFeO_3$- and $LaCrO_3$-based SOEC cathodes, suggesting that their bulk structures were stable under electrochemical CO_2 reduction conditions. To characterize the near surface region of the perovskites, HR-XPS was used before and after electrochemical testing. No significant changes were observed for Fe 2*p*, Co 2*p* and Cr 2*p* core level binding spectra of $LaCoO_3$, $LaFeO_3$ and $LaCrO_3$ before and after electrochemical testing (Figs. 5b1, 5b2 and 5b4, respectively). However, in the case of $LaNiO_3$, changes in the Ni 3*p* core binding spectra were observed with the appearance of a new feature at 72 eV in Fig. 5b3 after electrochemical testing. In addition, a slight shift in peak position for the Ni 3*p* core level binding energy (shown in green highlighted region in Fig. 5b3) also occurred. These changes could be due to the decomposition of $LaNiO_3$ to NiO and La_2O_3 (as suggested by XRD), leading to the presence of Ni and La cations in different chemical environments. A shift of the main Ni 3*p* binding energy peak to lower binding energies has been reported to be a sign of reduction.[50,51] The appearance of the new feature at 72 eV could be linked both to a satellite peak of Ni^{2+} oxidation state[52] and/or to the decreased intensity of the Ni^{3+} feature, which some references locate at around 71 eV.[53–55] Independent of the slightly different interpretations of the Ni 3*p* data, the XPS results were consistent with the findings from XRD, suggesting that $LaNiO_3$ was the only redox unstable perovskite under the considered electrochemical conditions.

Insights on the interaction of CO_2 with the $LaBO_3$ surfaces.—*Density function theory studies: CO_2 adsorption on $LaBO_3$ (B = Co, Fe, Ni) surfaces.*—To determine the factors that govern the difference in the electrochemical performance of $LaBO_3$ oxides for CO_2 reduction, the adsorption energetics of CO_2 on the perovskite surface were quantified using DFT calculations. As a first step, the preferential adsorption site of CO_2 on $LaCoO_3$ (110) was determined by systematically scanning through the parallel and perpendicular configurations of CO_2 relative to the surface. The corresponding site numbers and a top view of the corresponding configurations are shown in Fig. S4 in the Supplementary Material. The adsorption energies of the 10 distinct configurations are plotted in Fig. 6a. For most of these sites (configuration numbers 1–8 in Fig. 6a) a weak average adsorption energy of ~ -0.07 eV was found, indicating that CO_2 physisorbed on the surface. However, strong adsorption energies of -0.79 eV and -0.74 eV were obtained for configurations 9 and 10, respectively, indicating CO_2 was chemisorbed in these cases.

To better understand these results, we performed a charge density difference analysis and calculated the mean absolute charge transfer according to Eqs. 3 and 4 for adsorption configurations 9 and 10. We also analyzed configuration 4 as a direct comparable example since CO_2 adsorbs at the same site as configuration 10, but with a different orientation. For configuration 9, as shown in Fig. 6c, the CO_2 molecule chemisorbed on the surface with its carbon atom bonding with a lattice oxygen, and with both oxygens within the CO_2 molecule interacting with surface cobalt ions, forming a monodentate structure. There was an electron gain that was predominantly localized within the oxygen atoms from CO_2, leading to major electron losses from the surface Co cations and the carbon atom. As a result, the strong attraction stemming from an approximate charge transfer of 1.13 electrons led to a strong adsorption energy of -0.79 eV. The resulting C-O bond length was 1.35 Å, and the Co-O bond length of 2.10 Å, facilitating the direct charge transfer between the CO_2 molecule and the surface.

For configuration 10, CO_2 also bonded tightly with the surface. However, the bond length between the oxygen atoms from CO_2 and nearby Co cations were 1.91 Å and 2.97 Å, indicating a bidentate structure formation. Compared with configuration 9, a charge transfer of 1.04 electrons was obtained, resulting in a slightly weaker adsorption energy of -0.74 eV. In contrast, the CO_2 molecule physisorbed on the surface for configuration 4, with very weak dipole-dipole interactions between the adsorbate and the lattice O. As a result, only a small charge transfer of 0.12 electrons occurred with a 3.30 Å distance between the CO_2 molecule and the surface. Thus, both monodentate and bidentate carbonate structures were favorable on $LaCoO_3$ (110). These results show that both the perovskite surface 3*d* transition metal cations (i.e., Co) and the lattice oxygen species play a significant role in the adsorption and the activation of CO_2.

The adsorption energetics for CO_2 on $LaFeO_3$ (001) were also quantified as shown in Fig. 7a and b. The same bond length of 1.35 Å of C relative to the lattice O species indicates that CO_2 chemisorbs on this surface. The different adsorption energies of -0.52 eV and -0.34 eV for a monodentate (Fig. 7a) and a bidentate species (Fig. 7b) on this surface indicates that the adsorption energetics of CO_2 on $LaFeO_3$ (001) and $LaCoO_3$ (110) are different. The resulting Fe-O bond lengths of 2.07 Å between the oxygen from the CO_2 molecule and the nearby Fe cations yielded a monodentate species. As for the bidentate case, two different Fe–O bond lengths of 1.96 Å and 2.79 Å were obtained. Thus, both monodentate and bidentate carbonate structures were favorable on $LaFeO_3$ (001).

Similar studies were conducted on the $LaNiO_3$ (001) surface as shown in Fig. 7c. A very different bidentate carbonate structure with a strong adsorption energy of -0.92 eV was found in this case. This was because the termination of the $LaNiO_3$ (001) surface contained Ni, La and O ions, which was very different from $LaFeO_3$ (001) or $LaCoO_3$ (110) that only had O and the transition metal (Fe or Co) cations that were exposed on the surface. For $LaNiO_3$ (001), a bond length of 1.37 Å was obtained between the carbon atom of CO_2 and the surface oxygen atom, while a bond length of 2.67 Å was obtained between the lanthanum cation and the oxygen of CO_2, leading to a tilt angle of 62.34° with respect to the surface plane.

To probe the effect of O vacancies on $LaBO_3$ perovskite surfaces (the experimentally measured δ's ranged from 0.017–0.026 for these perovskites, as discussed above), we systematically removed one oxygen atom per unit cell from the surfaces and calculated the corresponding CO_2 adsorption energies (as shown in Fig. S5). The structures resulting in the most energetically favorable binding of CO_2 are shown in Fig. 8. We found that the oxygen defects played an important role in the adsorption energetics of CO_2, which led to adsorption energies that were comparable or greater than those on the stoichiometric surfaces. It is also clear that the presence of oxygen vacancies can alter the relative reactivity of a given surface and thus the energetics of CO_2 reduction do not only depend uniquely on the nature of the B-site. For example, on a stoichiometric $LaFeO_3$ (001) surface, the adsorption strength of CO_2 is weaker as compared to $LaNiO_3$ (001) and $LaCoO_3$ (110). However, in the presence of an oxygen vacancy, the adsorption strength of CO_2 on $LaFeO_3$ (001) is greater than when it chemisorbs on $LaNiO_3$ (001) and $LaCoO_3$ (110). We remark that the results regarding the chemisorption of CO_2 in the presence of oxygen vacancies are also more in line with the experimental observations, which indicate that activity toward reduction of CO_2 is higher for $LaFeO_3$ as compared to $LaNiO_3$.

As such, both the nature of the B-site and oxygen vacancy distribution must be considered to arrive at a predictive model for such complex systems. These results agree with the previous reports in that the CO_2 adsorption energies will change in the presence of surface oxygen vacancies because of the induced imperfections to

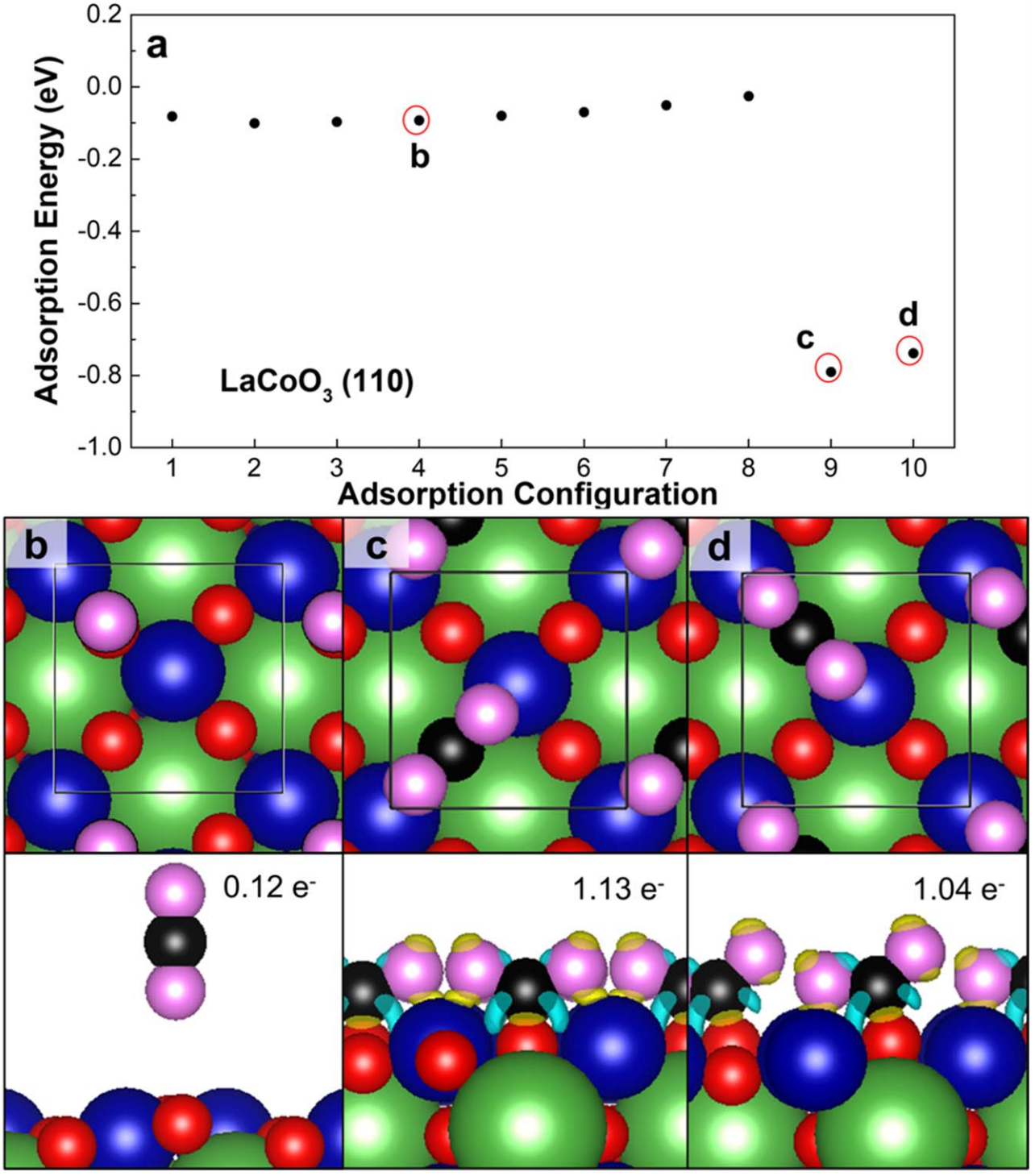

Figure 6. (a) The adsorption energies of 10 possible configurations for a CO_2 molecule on the $LaCoO_3$ (110) surface. (b)–(d) Top and side views for configurations b, c and d as marked by the red circles in panel a. The La, Co, C, lattice O and O within a CO_2 molecule are represented by green, blue, black, red, and pink spheres, respectively. The areas indicated in yellow represent those of electron gain while those in blue are those of electron loss upon the adsorption of the CO_2 at an isosurface level of 0.01 electrons/Bohr^3.

the surface basicity and the ability of defects to accept electrons from adsorbates.[56,57] However, we also note that the distribution of oxygen defects on a given surface will depend sensitively on the oxygen and the CO_2 pressures. As such, a first principles-based phase diagram needs to be constructed where oxygen vacancy concentration as well as the CO_2 coverage are systematically varied. We anticipate that further fundamental insights into CO_2 reduction activity trends will result by considering these additional complexities, which will be benchmarked in our future work.

To understand how the weakly physiosorbed gas phase CO_2 transfers into the strongly chemisorbed monodentate or bidentate structures on $LaBO_3$ (B = Ni, Co, Fe), we determined its corresponding minimum energy pathway, as shown in Fig. S6 in the Supplementary Material. We present $LaCoO_3$ (110) as an

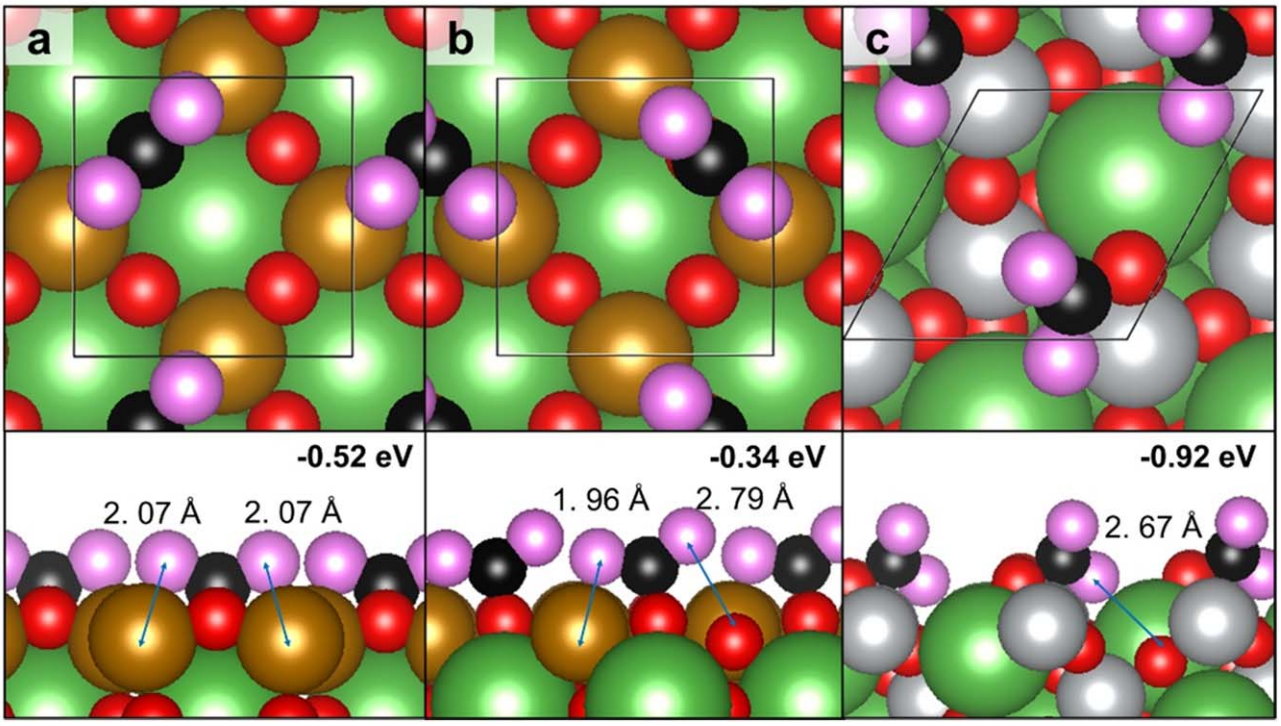

Figure 7. Top and side views for (a) the monodentate and (b) the bidentate CO_2 chemisorbed structure on $LaFeO_3$ (001), and (c) the bidentate CO_2 chemisorbed structure on $LaNiO_3$ (001). The La, Fe, Ni, C, lattice O and O within a CO_2 molecule are represented by green, bronze, silver, black, red, and pink spheres, respectively.

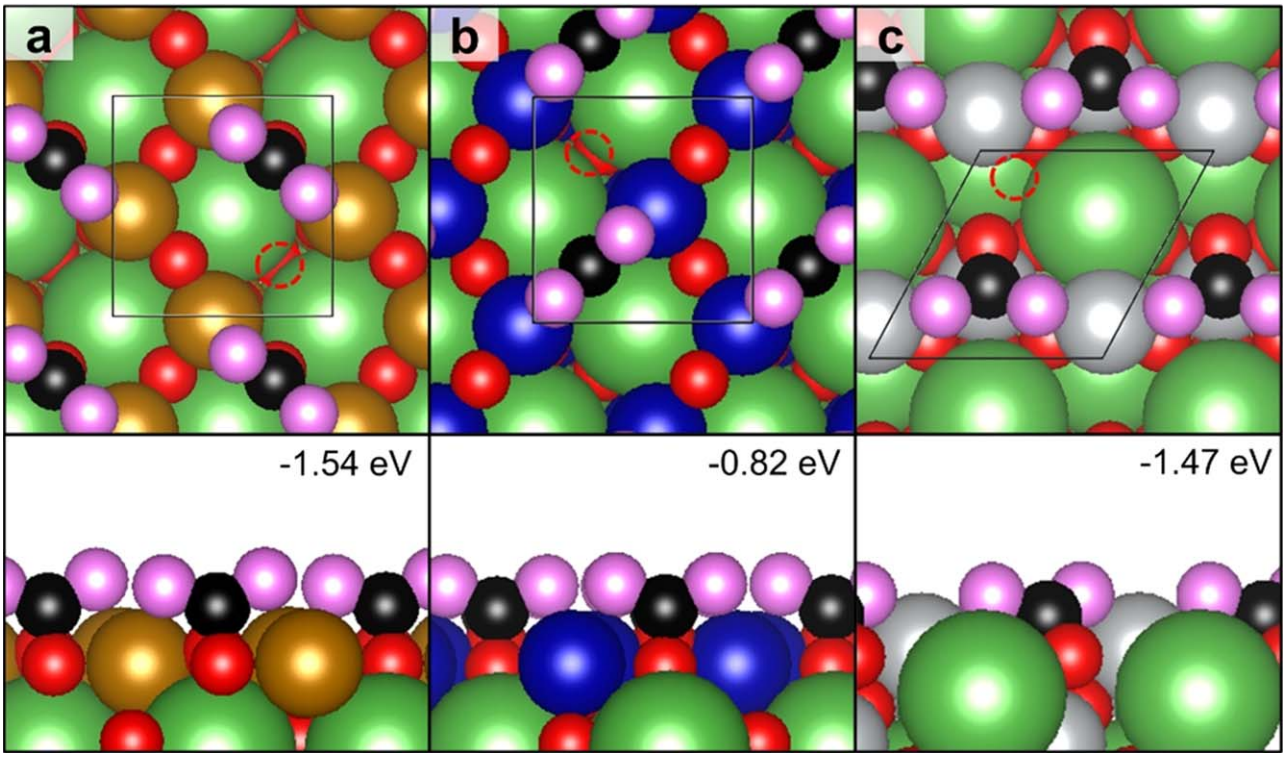

Figure 8. Top and side view for the most energetically favorable structures involving the chemisorption of CO_2 on (a) $LaFeO_3$ (001) (b) $LaCoO_3$ (110) and (c) $LaNiO_3$ (001) with one oxygen vacancy (marked by red dash circle). The La, Fe, Co, Ni, C, lattice O and O within a CO_2 molecule are represented by green, bronze, blue, grey, black, red, and pink spheres, respectively.

example to illustrate the details of the chemisorption process, as shown in Fig. 9. The energetics were calculated for each step. The initial, transition, and final states are denoted as IS, TS, and FS, respectively. A 3.30 Å gap between the CO_2 molecule and the surface with a weak adsorption energy of −0.08 eV indicates that CO_2 physisorbs on the surface with two oxygen atoms right above two adjacent Co cations. When CO_2 approaches the surface, one oxygen of the CO_2 molecule interacts with a cobalt cation (Fig. 9b), leading to a tilted configuration. This coordination further results in a 0.26 eV activation barrier, in which the carbon atom of CO_2 starts to

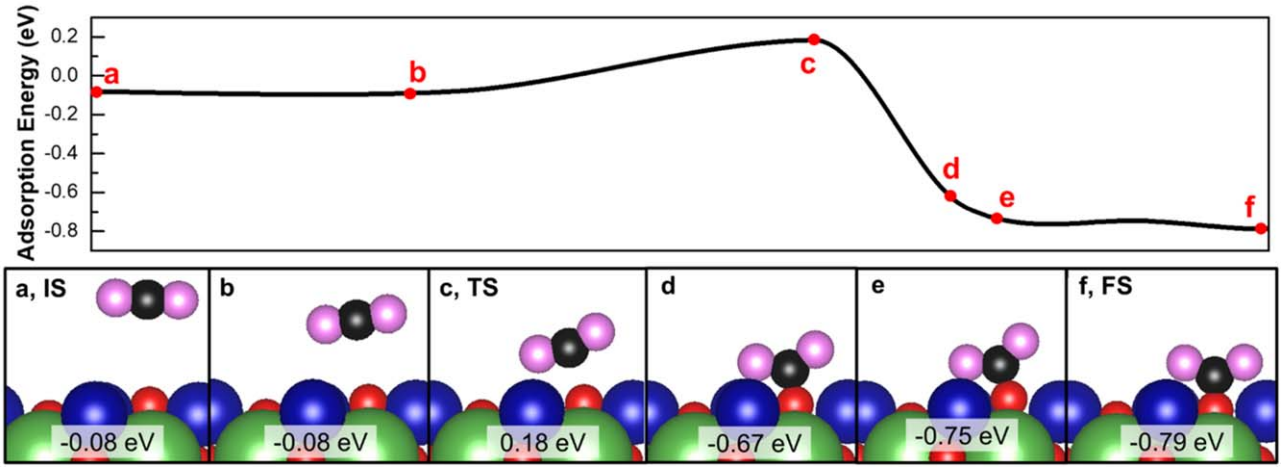

Figure 9. Minimum energy pathway and corresponding configurations regarding the activation of CO_2 to form a monodentate structure on $LaCoO_3$ (110). The adsorption energy is calculated for each step. The initial state, transition state and final state are denoted as IS, TS and FS, respectively. The La, Co, C, lattice O and O within a CO_2 molecule are represented by green, blue, black, red, and pink spheres, respectively.

interact with a lattice surface oxygen ion (Fig. 9c) leading to a CO_2-O monodentate structure. The overall CO_2 chemisorption process of CO_2 was exothermic by 0.71 eV.

In situ CO_2 DRIFT studies on $LaBO_3$ perovskites.—CO_2 binding on the perovskite surface as a function of the B-site composition was also probed experimentally via *in situ* CO_2 DRIFT studies. The measurements were conducted on $LaBO_3$ oxides exposed to CO_2 at 300 °C and the carbonaceous surface species formed from the chemical interaction of CO_2 with the oxide surface were identified by conducting DRIFT measurements at room temperature (Figs. 10 and S8). The interactions of CO_2 with the

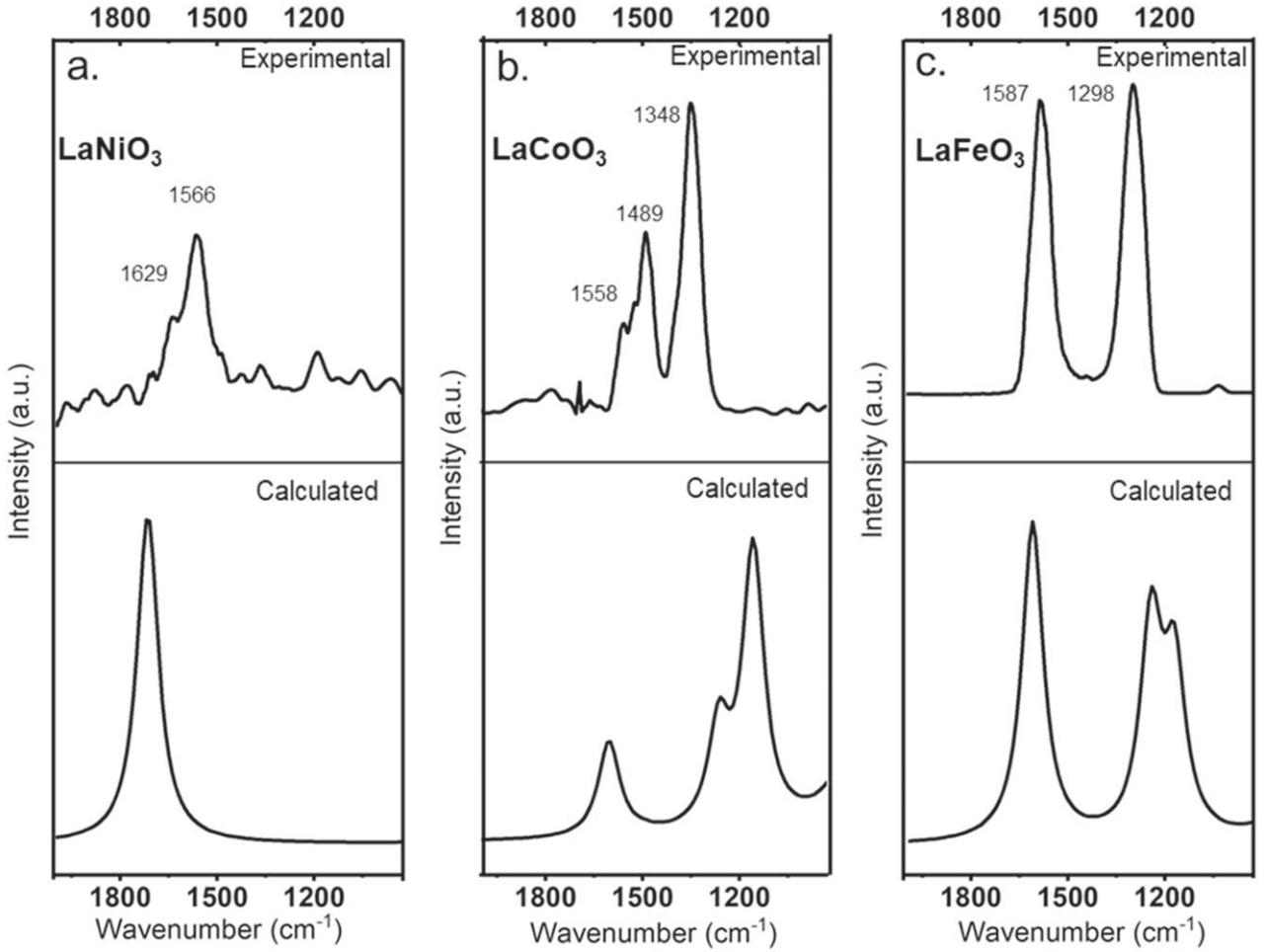

Figure 10. Experimentally measured CO_2 DRIFTS and calculated IR spectra of the carbonate O−C−O stretching region for: (a). $LaNiO_3$ (b). $LaCoO_3$ (c). $LaFeO_3$.

$LaBO_3$ perovskite surfaces yielded main vibration bands between 1800 and 1100 cm^{-1} associated with surface carbonate species.[58–60] The vibrational bands in the region of 1550–1100 cm^{-1} were consistent with main or secondary vibrations for monodentate and bidentate carbonate surface species, respectively, while the bands in the region of 1800–1550 cm^{-1} were associated with the main vibrations from bidentate carbonates.[61,62] To confirm these assignments and also to benchmark the theoretical binding sites for CO_2, the measured CO_2 DRIFT spectra were compared with the computed vibrational fingerprints from DFT (Fig. 10). The details of the vibration frequency calculations are included in the Supplementary Material. Figure 10a shows that in the case of $LaNiO_3$, vibrational bands were observed and computed at frequencies >1560 cm^{-1}, consistent with the main vibration of the bidentate carbonate surface species. Conversely, in the case of $LaCoO_3$ surface, monodentate carbonate species with features at 1348 and 1489 cm^{-1} (where splitting is less than 200 cm^{-1}) associated with symmetric O–C–O and asymmetric O–C–O vibrational modes were predominately observed experimentally. The weak contribution around 1558 cm^{-1} agreed with the formation of surface bidentate carbonate species for asymmetric (O–C–O) stretching.[62–65] The experiemtally observed combination of monodentate and bidentate carbonate surface species on $LaCoO_3$ were supported by the calculated IR spectra from DFT. In the case of $LaFeO_3$, the position of the bands at 1587 and 1298 cm^{-1} (where the splitting is around 300 cm^{-1}) indicated bicarbonate structures with asymmetric O−C−O and symmetric O−C−O vibrational modes. The band around 1300 cm^{-1} can also be associated with monodentate carbonate species. This is consistent with the calculated IR spectra from DFT which suggest that both monodentate and bidentate carbonate structures are energetically favorable on $LaFeO_3$ (001) (Fig. 10c, bottom plot). The simulated IR spectra do not change significantly if one simulates the IR spectra within a p (2 × 2) unit cell at the same CO_2 coverage of 1 ML, as can be seen by comparing the results shown in Fig. 10 for the p (1 × 1) unit cell with those for the p (2 × 2) unit cell shown in Fig. S7. The only noticeable change is that the relative intensities of the two peaks in the simulated spectrum of $LaFeO_3$ (001) for the p (2 × 2) unit cell are more in line with the experimental results, where the band around 1298 cm^{-1} has a higher intensity as compared to the band at 1587 cm^{-1}. These studies suggest consistency between the experimentally observed binding sites and those used theoretically to determine the energetics associated with CO_2 adsorption.

Conclusions

The influence of the B-site 3*d* transition metal cation of $LaBO_3$ perovskites on the electrochemical activity and Faradaic efficiency toward the production of CO from the electrochemical reduction of CO_2 in SOECs was investigated using a combination of chronoamperometric and impedance studies. The electrochemical performance of SOECs with $LaBO_3$-based cathodes under CO_2 reduction conditions followed a trend of $LaFeO_3$ > $LaCoO_3$ > $LaNiO_3$ > $LaCrO_3$. Among these $LaBO_3$ perovskites, $LaNiO_3$ was the least stable and decomposed under electrochemical CO_2 reduction conditions. *In situ* CO_2 DRIFT studies and DFT calculations suggested that both the nature of the B-site cation and the presence of oxygen surface vacancies in these perovskites played a critical role in the energetics of adsorption and reduction of CO_2. We found that an optimal oxophilic characteristic of the B-site 3*d* transition metal cations was required to tune the electrochemical performance. Theoretical analysis of the energetics of CO_2 adsorption suggested that adjacent oxygen surface vacancies to B-site cations, significantly contributed toward increasing the strength of CO_2 adsorption on these sites. These findings clearly suggest that in tuning the electrochemical catalytic properties of ABO_3 perovskites for CO_2 reduction to CO in SOECs, both the nature of the B-site cation and the oxygen non-stoichiometry (surface oxygen deficiency) should be considered. These findings are important toward devising ways to improve the performance of MIEC-based SOEC cathodes for this process.

Acknowledgments

The authors thank the primary financial support from the National Science Foundation Ceramics Program (Award Numbers DMR-1929314 and DMR-1929306). This work was partially funded by the Joint Center for Deployment and Research in Earth Abundant Materials (JCDREAM) in Washington State. This work used the Extreme Science and Engineering Discovery Environment (XSEDE),[66] which is supported by National Science Foundation grant number ACI-1548562. Additional computational resources were provided by the Kamiak HPC under the Center for Institutional Research Computing at Washington State University. The authors also thank the Lumigen Instrument Center at Wayne State University for the use of the X-ray diffraction (National Science Foundation MRI-1427926), X-ray photoelectron spectroscopy (National Science Foundation MRI-1849578) and electron microscopy facilities (National Science Foundation MRI-0216084). The Pacific Northwest National Laboratory is operated by Battelle for the U.S. DOE.

ORCID

Reinhard Denecke https://orcid.org/0000-0003-1065-5791
Jean-Sabin McEwen https://orcid.org/0000-0003-0931-4869
Eranda Nikolla https://orcid.org/0000-0002-8172-884X

References

1. O. Hoegh-Guldberg et al., *Science*, **365**, 1372 (2019).
2. Y. F. Song, X. M. Zhang, K. Xie, G. X. Wang, and X. H. Bao, *Adv. Mater.*, **31**, 1902033 (2019).
3. X. Zhang, Y. Song, G. Wang, and X. Bao, *J. Energy Chem.*, **26**, 839 (2017).
4. W. Yue et al., *Nano Energy*, **62**, 64 (2019).
5. X.-K. Gu, J. S. A. Carneiro, and E. Nikolla, *Ind. Eng. Chem. Res.*, **56**, 6155 (2017).
6. J. Carneiro, X.-K. Gu, E. Tezel, and E. Nikolla, *I Ind. Eng. Chem. Res*, **59**, 15884 (2020).
7. S. Liu, Q. Liu, and J.-L. Luo, *J. Mater. Chem. A*, **4**, 17521 (2016).
8. S. Ding, M. Li, W. Pang, B. Hua, N. Duan, Y.-Q. Zhang, S.-N. Zhang, Z. Jin, and J.-L. Luo, *Electrochim. Acta*, **335**, 135683 (2020).
9. S. Liu, Q. Liu, and J.-L. Luo, *ACS Catal.*, **6**, 6219 (2016).
10. S. Wang, A. Inoishi, J.-E. Hong, Y.-W. Ju, H. Hagiwara, S. Ida, and T. Ishihara, *J. Mater. Chem. A*, **1**, 12455 (2013).
11. T. Ishihara, K.-T. Wu, and S. Wang, *ECS Trans.*, **66**, 197 (2015).
12. M. Torrell, S. García-Rodríguez, A. Morata, G. Penelas, and A. Tarancón, *Faraday Discuss.*, **182**, 241 (2015).
13. R. Xing, Y. Wang, Y. Zhu, S. Liu, and C. Jin, *J. Power Sources*, **274**, 260 (2015).
14. S. Li, Y. Li, Y. Gan, K. Xie, and G. Meng, *J. Power Sources*, **218**, 244 (2012).
15. X.-K. Gu, J. S. A. Carneiro, S. Samira, A. Das, N. M. Ariyasingha, and E. Nikolla, *J. Am. Chem. Soc.*, **140**, 8128 (2018).
16. Q. Ji, L. Bi, J. Zhang, H. Cao, and X. S. Zhao, *Energy Environ. Sci.*, **13**, 1408 (2020).
17. Y. Chen, H. Téllez, M. Burriel, F. Yang, N. Tsvetkov, Z. Cai, D. W. McComb, J. A. Kilner, and B. Yildiz, *Chem. Mater.*, **27**, 5436 (2015).
18. D. Lee, Y.-L. Lee, A. Grimaud, W. T. Hong, M. D. Biegalski, D. Morgan, and Y. Shao-Horn, *J. Mater. Chem. A*, **2**, 6480 (2014).
19. X. Yue and J. Irvine, *Solid State Ion.*, **225**, 131 (2012).
20. X. Zhang, Y. Song, F. Guan, Y. Zhou, H. Lv, Q. Liu, G. Wang, and X. Bao, *J. Power Sources*, **400**, 104 (2018).
21. S. Xu, S. Li, W. Yao, D. Dong, and K. Xie, *J. Power Sources*, **230**, 115 (2013).
22. C. Ruan, K. Xie, L. Yang, B. Ding, and Y. Wu, *Int. J. Hydrog. Energy*, **39**, 10338 (2014).
23. S.-E. Yoon, J.-Y. Ahn, B.-K. Kim, and J.-S. Park, *Int. J. Hydrog. Energy*, **40**, 13558 (2015).
24. H. Li, G. Sun, K. Xie, W. Qi, Q. Qin, H. Wei, S. Chen, Y. Wang, Y. Zhang, and Y. Wu, *Int. J. Hydrog. Energy*, **39**, 20888 (2014).
25. J. Mizusaki, T. Sasamoto, W. R. Cannon, and H. K. Bowen, *J. Am. Ceram. Soc.*, **66**, 247 (1983).
26. A. Aguadero, L. Fawcett, S. Taub, R. Woolley, K.-T. Wu, N. Xu, J. A. Kilner, and S. J. Skinner, *J. Mater. Sci.*, **47**, 3925 (2012).
27. A. K. Opitz et al., *ACS Appl. Mater. Interfaces*, **9**, 35847 (2017).
28. B. H. Ren, E. Croiset, and L. Ricardez-Sandoval, *J. Catal.*, **383**, 273 (2020).
29. S. Samira, X.-K. Gu, and E. Nikolla, *ACS Catal.*, **9**, 10575 (2019).
30. J. S. A. Carneiro, J. Williams, A. Gryko, L. P. Herrera, and E. Nikolla, *ACS Catal.*, **10**, 516 (2020).
31. G. Kresse and J. Hafner, *Phys. Rev. B*, **47**, 558 (1993).
32. B. Hammer, L. B. Hansen, and J. K. Nørskov, *Phys. Rev. B*, **59**, 7413 (1999).
33. G. Kresse and D. Joubert, *Phys. Rev. B*, **59**, 1758 (1999).
34. K. Lejaeghere et al., *Science*, **351**, aad3000 (2016).
35. K. Momma and F. Izumi, *J. Appl. Crystallogr.*, **44**, 1272 (2011).
36. J. B. Goodenough, *J. Phys. Chem. Solids*, **6**, 287 (1958).
37. J. Kanamori, *J. Phys. Chem. Solids*, **10**, 87 (1959).

38. J. B. Goodenough, *Phys. Rev.*, **100**, 564 (1955).
39. M. T. Curnan and J. R. Kitchin, *J. Phys. Chem. C*, **118**, 28776 (2014).
40. K. Saritas, J. T. Krogel, S. Okamoto, H. N. Lee, and F. A. Reboredo, *Phys. Rev. Mater.*, **3**, 124414 (2019).
41. K. Kleveland, N. Orlovskaya, T. Grande, A. M. M. Moe, M.-A. Einarsrud, K. Breder, and G. Gogotsi, *J. Am. Ceram. Soc.*, **84**, 2029 (2001).
42. G. Gou, I. Grinberg, A. M. Rappe, and J. M. Rondinelli, *Phys. Rev. B*, **84**, 144101 (2011).
43. D. Mutter, R. Schierholz, D. F. Urban, S. A. Heuer, T. Ohlerth, H. Kungl, C. Elsässer, and R.-A. Eichel, *Chem. Mater.*, **33**, 9473 (2021).
44. V. Vulchev, L. Vassilev, S. Harizanova, M. Khristov, E. Zhecheva, and R. Stoyanova, *J. Phys. Chem. C*, **116**, 13507 (2012).
45. W. Zhou and J. Sunarso, *J. Phys. Chem. Lett.*, **4**, 2982 (2013).
46. S. She, J. Yu, W. Tang, Y. Zhu, Y. Chen, J. Sunarso, W. Zhou, and Z. Shao, *ACS Appl. Mater. Interfaces*, **10**, 11715 (2018).
47. Z. El-Fadli, M. R. Metni, F. Sapiña, E. Martinez, J. V. Folgado, D. Beltrán, and A. Beltrán, *J. Mater. Chem.*, **10**, 437 (2000).
48. N. Ulumuddin, F. Che, J. I. Yang, S. Ha, and J. S. McEwen, *Catalysts*, **11**, 271 (2021).
49. S. Liu, Q. Liu, and J.-L. Luo, *J. Mater. Chem. A*, **5**, 2673 (2017).
50. G. Vovk, X. Chen, and C. A. Mims, *J. Phys. Chem. B*, **109**, 2445 (2005).
51. J. S. Choi et al., *ACS Appl. Electron. Mater.*, **1**, 1952 (2019).
52. Z. Liu, S. Yao, A. Johnston-Peck, W. Xu, J. A. Rodriguez, and S. D. Senanayake, *Catal. Today*, **311**, 74 (2018).
53. M. Saghayezhian, Z. Wang, H. Guo, Y. Zhu, E. Plummer, and J. Zhang, *Phys. Rev. B*, **95**, 165434 (2016).
54. M. Taeño, J. Bartolomé, L. Gregoratti, P. Modrzynski, D. Maestre, and A. Cremades, *Cryst. Growth Des.*, **20**, 4082 (2020).
55. V. Hien-Hoang, N. K. Chung, and H. J. Kim, *Sci Rep.*, **11** (2021).
56. K. Nomura, Y. Ujihira, T. Hayakawa, and K. Takehira, *Appl. Catal. A: Gen.*, **137**, 25 (1996).
57. T. Sakpal and L. Lefferts, *J. Catal.*, **367**, 171 (2018).
58. D. J. Deka, J. Kim, S. Gunduz, M. Aouine, J. M. M. Millet, A. C. Co, and U. S. Ozkan, *Appl. Catal. B: Environ.*, **286**, 119642 (2021).
59. G. Busca and V. Lorenzelli, *Mater. Chem.*, **7**, 89 (1982).
60. J. Kim, M. Ferree, S. Gunduz, J.-M. M. Millet, M. Aouine, A. C. Co, and U. S. Ozkan, *J. Mater. Chem. A*, **10**, 2483 (2022).
61. K. Sutthiumporn, T. Maneerung, Y. Kathiraser, and S. Kawi, *Int. J. Hydrog. Energy*, **37**, 11195 (2012).
62. L. G. Tejuca, C. H. Rochester, J. L. G. Fierro, and J. M. D. Tascón, *J. Chem. Soc., Faraday Trans. 1*, **80**, 1089 (1984).
63. A. Hakim, T. S. Marliza, N. M. Abu Tahari, R. W. N. Wan Isahak, R. M. Yusop, W. M. Mohamed Hisham, and A. M. Yarmo, *Ind. Eng. Chem. Res.*, **55**, 7888 (2016).
64. L. Luo, R. Hernandez, X. D. Zhou, and H. Yan, *Appl. Catal. A: Gen.*, **624**, 118330 (2021).
65. D. Hauser, A. Nenning, A. K. Opitz, B. Klötzer, and S. Penner, *Rev. Sci. Instrum.*, **91**, 084104 (2020).
66. J. Towns et al., *Comput. Sci. Eng.*, **16**, 62 (2014).